Journal of Advanced Ceramics
先进陶瓷
ISSN 2226-4108
CN 10-1154/TQ
清華大學出版社 Tsinghua University Press
SciOpen

J Adv Ceram 2026, **15**: 9221405

https://doi.org/10.26599/JAC.2026.9221405

Research Article

Acid corrosion of high-entropy ceramics: Insights from an entropy-stabilized oxide model system

Ying Zhao, Ji-Xuan Liu*, Guo-Jun Zhang*

State Key Laboratory of Advanced Fiber Materials, College of Materials Science and Engineering, College of Physics, Donghua University, Shanghai 201620, China

*Corresponding author.

E-mail: J.-X. Liu, jxliu@dhu.edu.cn;

G.-J. Zhang, gjzhang@dhu.edu.cn

Received: October 28, 2026; Revised: November 8, 2026; Accepted: November 8, 2026

©The Author(s) 2026

Just Accepted

清華大學出版社 Tsinghua University Press | SciOpen

Abstract

High-entropy engineering has emerged as a promising strategy for designing compositionally complex materials with enhanced structural stability. However, it remains unclear whether high-entropy structures intrinsically improve corrosion resistance. Herein, an entropy-stabilized rock-salt (MgCoNiCuZn)O (HEO) high-entropy oxide was selected as a model system and compared with a mechanically mixed oxide (MO) consisting of MgO, Co_3O_4, NiO, CuO, and ZnO mixed at equimolar metal-cation ratios. Despite the same nominal cation composition, MO consists of independent oxide phases, whereas HEO forms a single-phase rock-salt solid solution. Hydrochloric-acid immersion experiments reveal distinctly different corrosion pathways. MO undergoes pronounced elemental dissolution selectivity, with Mg-, Zn-, and Cu-containing phases preferentially removed while Ni- and Co-containing phases are relatively retained. In contrast, HEO exhibits substantially reduced elemental dissolution selectivity, consistent with coupled multielement dissolution within the common lattice. Moreover, the corrosion response of HEO strongly depends on acid concentration. HEO exhibits lower net mass loss than MO in 1 M HCl, whereas its degradation becomes substantially more severe in 6 M HCl and the net mass loss exceeds that of MO. Residual HEO retains the multielement rock-salt structure while developing interfacial stratification and localized Cu/Cl-containing corrosion-derived species. These results show that high-entropy solid-solution formation modifies corrosion pathways rather than universally enhancing corrosion resistance, highlighting the coupled roles of phase constitution, constituent chemistry, and environmental aggressiveness in designing corrosion-resistant ceramics.

Just Accepted

Keywords:

High-entropy ceramics; Entropy-stabilized oxide; Aqueous corrosion; Selective dissolution; Phase constitution; Hydrochloric acid

1 Introduction

Since the emergence of high-entropy alloys (HEAs) in 2004 [1,2], high-entropy engineering has evolved into a broad strategy for designing compositionally complex materials. The concept has subsequently been extended from metallic systems to ceramics, including oxides [3], carbides [4], nitrides [5], borides [6], and silicides [7,8], leading to the development of high-entropy ceramics (HECs) [9]. Their properties are commonly interpreted through four core effects, namely high-entropy effect, sluggish diffusion effect, severe lattice distortion effect, and cocktail effect [10–12]. However, these effects are not universal descriptors of improved performance, because their influence depends strongly on composition, crystal structure, bonding, and service environment.

Corrosion provides a clear example. The corrosion behavior of HEAs in aqueous environments shows that high-entropy design does not necessarily improve environmental stability [13–16]. For example, ICP-AES analysis on the CoCrFeMnNi Cantor alloy revealed distinct dissolution behaviors among constituent elements during localized corrosion, with Cr playing a critical role in passive film regeneration and repassivation processes [17]. Studies on $CoCrFeNiMo_x$ HEAs showed that phase constitution, together with the competition between Cr_2O_3 enrichment and selective dissolution, strongly influence corrosion behavior [18]. Furthermore, chloride concentration and temperature markedly alter passive-film stability and pitting susceptibility of CoCrFeMnNi HEA [19]. Together, these studies indicate that in HEAs, corrosion is governed by phase constitution, passive-film evolution,

Just Accepted

element-specific dissolution, and environmental conditions, rather than by configurational entropy alone.

Similar behavior has been reported for HECs. In high-temperature oxidation, a common form of dry corrosion, equimolar multicomponent carbides with identical ideal configurational entropy can show different oxidation resistance [20–22]. Specific constituents can also promote oxide-scale densification in high-entropy carbide-based composites and multicomponent diborides [23,24]. In CaO-MgO-Al_2O_3-SiO_2 (CMAS) melt and molten-salt environments, the corrosion behavior of high-entropy rare-earth oxide ceramics remains sensitive to constituent chemistry and reaction-product evolution [25–33]. Collectively, these studies show that the conclusion drawn for HEAs also holds for HECs, in that high-entropy solid-solution formation can modify degradation pathways, but across both HEAs and HECs the response is governed by phase constitution, constituent chemistry, interfacial reactions, and environment, rather than by configurational entropy alone.

Beyond the high-temperature and molten-salt environments discussed above, HECs can be used as corrosion-resistant components in chemical equipment, including pipe linings and seals, where they will be exposed to acidic or alkaline media. Understanding their chemical stability in such environments is therefore important for designing corrosion-resistant materials. To date, however, aqueous-corrosion studies of HECs remain limited. In neutral solutions, static leaching tests on $A_2B_2O_7$-type HECs for radioactive-waste immobilization showed that the synergy between sluggish diffusion effect, severe lattice distortion effect, and the intrinsic element–oxygen bonding strength governs elemental release [34]. Nevertheless, such tests primarily quantify leach rates under fixed conditions and do not resolve element-specific dissolution pathways or phase-associated differences.

Just Accepted

Systematic aqueous-corrosion studies of HECs, particularly in acidic and alkaline media and at matched nominal cation compositions, therefore remain scarce, especially those that resolve element-specific dissolution and examine phase-associated differences.

Entropy-stabilized oxides offer a platform to study how high-entropy solid-solution structures influence corrosion. Rost et al. [3] reported the reversible entropy-driven stabilization of (MgCoNiCuZn)O (HEO) as a single-phase rock-salt solid solution. Unlike many compositionally complex ceramics whose single-phase formation is primarily driven by a sufficiently negative enthalpy of mixing rather than by entropy stabilization [35], the entropy-stabilized HEO system offers a well-defined model for comparing the same constituent cations accommodated in separate oxide phases versus a common rock-salt lattice. This model allows us to examine how phase constitution influences element-specific dissolution in multicomponent oxides with matched nominal cation compositions under aqueous corrosion conditions. On that basis, it becomes possible to ask whether a reduced elemental dissolution selectivity, necessarily translates into improved corrosion resistance. It also remains unclear how environmental aggressiveness affects elemental dissolution, residual-solid evolution, and overall degradation.

To address these questions, we selected the entropy-stabilized HEO as a model system and compared it with a mechanically mixed oxide (MO) containing MgO, Co_3O_4, NiO, CuO, and ZnO at equimolar metal-cation ratios. The individual oxides were also examined as constituent-level references under the same conditions. Although the two materials share the same nominal cation composition, they differ fundamentally in how the cations are accommodated: MO contains independent oxide phases, HEO is a single-phase rock-salt solid solution in which the five cations share a common sublattice. By

Just Accepted

comparing net mass loss, element-specific dissolution, residual-phase evolution, and post-corrosion morphology in 1 and 6 M HCl, this study examines how constituent-specific dissolution is expressed in distinct oxide phases, how it changes when the same cations share a common lattice, and how these changes translate into corrosion performance under different environmental aggressiveness.

2 Experimental

2.1. Sample preparation

MO powder and HEO powder with the same nominal equimolar metal-cation composition were prepared for corrosion comparison. Commercial MgO, Co_3O_4, NiO, CuO, and ZnO powders (analytical reagent grade) were used as starting materials. The molar ratio of Mg: Co: Ni: Cu: Zn was fixed at 1: 1: 1: 1: 1 for all samples. The MO powder was prepared by directly mixing the five oxide powders at an equimolar metal-cation ratio without further milling or heat treatment, to accurately control the stoichiometric proportions and preserve a mechanically mixed, non-reacted reference state for comparison. The HEO powder was synthesized via a conventional solid-state reaction route. The raw oxide powders were mixed by planetary ball milling at 560 rpm for 10 h using ZrO_2 balls and ethanol as the solvent. The ball-to-powder mass ratio was 6:1, and 3 and 5 mm balls were used in equal masses. After drying, the mixed powders were sieved through a 200-mesh sieve and pressed into pellets. The pellets were heated to 950 °C at 5 °C min^{-1}, held for 15 h in air, and then furnace-cooled to room temperature. After calcination, the pellets were crushed, re-ground, and sieved (200 mesh) to obtain final powders for corrosion experiments. Fig. 1 illustrates the sample preparation scheme. Both samples underwent identical corrosion testing conditions to ensure comparability.

Just Accepted

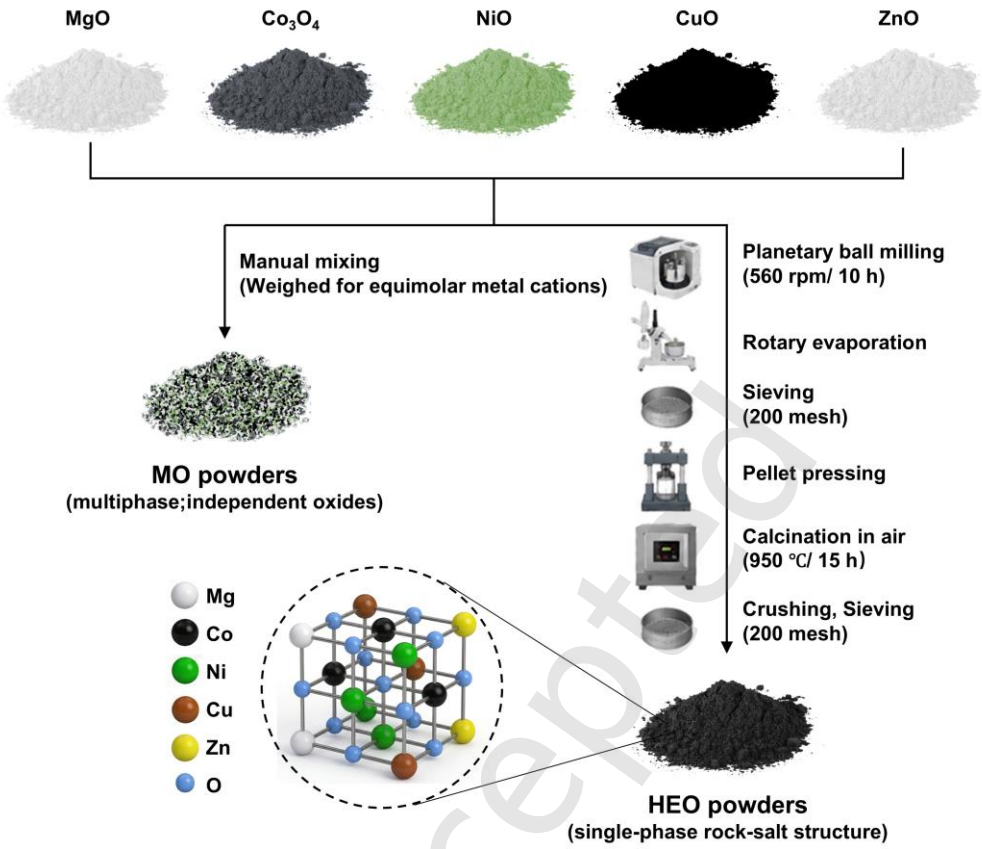


Fig. 1 Schematic illustration of the preparation routes for MO and HEO powders.

2.2. Corrosion experiments

The acid corrosion behavior of the oxide powders was evaluated using static immersion tests. The amounts of powder and solution were selected with reference to GB/T 2835-1998 (Test method for acid resistance of vitrified claypipe). Fig. 2 illustrates the experimental scheme. HCl solutions at 1 M and 6 M were prepared as corrosive media to examine the influence of acid concentration on corrosion behavior. For each test, an amount of MO powder or HEO powder corresponding to 0.0125 mol total metal cations was accurately weighed and immersed in 25 mL of HCl solution in a centrifuge tube. Individual MgO, Co_3O_4, NiO, CuO, and ZnO powders were additionally tested under the same conditions as constituent-level references. All immersion experiments were conducted in triplicate under static conditions for 12 h at an ambient temperature of 25 °C and a relative humidity of 65%.

Just Accepted

After immersion, the solid and liquid phases were separated by centrifugation at 7000 rpm for 3 min. The supernatant (corrosion solution) was collected for inductively coupled plasma optical emission spectroscopy (ICP-OES) to determine the dissolved concentrations of Mg, Co, Ni, Cu, and Zn. The solid residue (corroded powder) was washed three times with deionized water via repeated centrifugation to remove residual acid. The wash solutions were not included in the ICP-OES analysis. The cleaned powder was then dried at 60 °C to constant mass, as verified by repeated weighing, and the final mass was used to calculate the net mass loss.

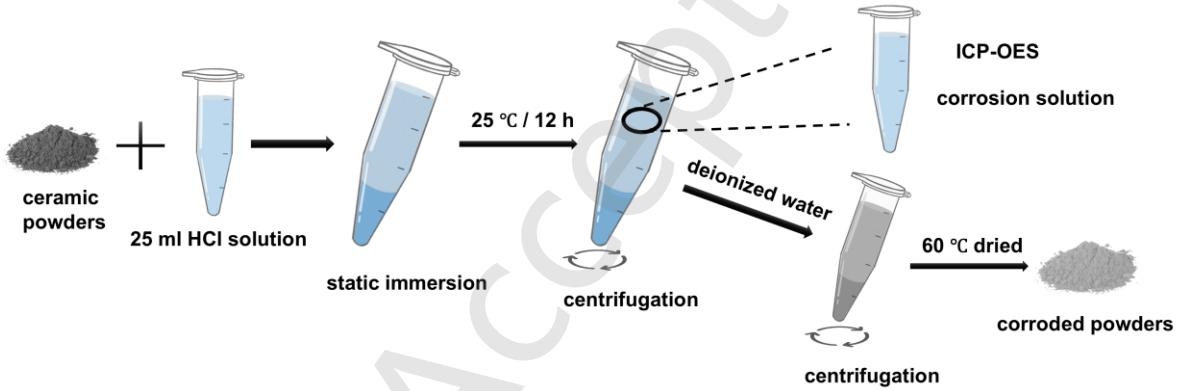


Fig. 2 Schematic of the corrosion testing procedure.

2.3. Characterizations

Phase identification of the powder samples before and after corrosion was performed by X-ray diffraction (XRD, MiniFlex, Rigaku, Japan) with Cu Kα radiation at 40 kV and 15 mA over a 2θ range from 10° to 90°. The surface morphology and elemental distribution of the samples before and after corrosion were examined by scanning electron microscopy with energy-dispersive X-ray spectroscopy (SEM-EDS, GeminiSEM 560, ZEISS, Germany). Samples were sputter-coated with gold prior to observation to ensure sufficient electrical conductivity. The concentrations of dissolved metal ions in the corrosion solutions were quantified by inductively coupled plasma optical emission spectroscopy

Just Accepted

(ICP-OES, Prodigy Plus, Teledyne Leeman Labs, USA). Before analysis, the immersion supernatants were diluted 80× with deionized water. Calibration was performed over a concentration range of 0.01-100 mg/L. The measured ion concentrations were used to evaluate the dissolution behavior of individual elements during corrosion. The pH values of the HCl solutions before and after corrosion were measured using a calibrated pH meter (FE28-Standard, Mettler-Toledo, Switzerland) equipped with a combination pH electrode (LE410) to assess changes in bulk solution acidity after immersion.

3 Results and Discussion

3.1. Initial phase constitution and structural characteristics

Figure 3 shows the initial phase constitution and microstructure of MO and HEO. The XRD patterns (Fig. 3a) confirm that MO consists of five constituent oxide phases, including MgO, Co_3O_4, NiO, CuO, and ZnO. In contrast, HEO exhibits a single-phase solid solution with a rock-salt structure. Despite possessing the same nominal cation composition, MO and HEO exhibit fundamentally different phase constitutions.

SEM observations (Fig. 3b, c) further reveal distinct particle characteristics between the two materials. MO contains constituent oxide particles with heterogeneous morphologies and sizes. HEO consists of irregular crushed particles with a comparatively more uniform morphology. SEM-based particle size analysis further confirms that HEO exhibits a larger characteristic particle size than MO, with average particle sizes of 0.74 and 0.27 μm, respectively (Fig. S1).

The elemental distribution further highlights the difference between the two systems. As shown by the EDS elemental maps (Fig. 3d, e), Mg, Co, Ni, Cu, and Zn in MO are spatially associated with different particles, consistent with the coexistence of compositionally distinct oxide phases. In contrast,

Just Accepted

all five elements are distributed throughout the examined HEO particles without the pronounced elemental separation observed in MO. Together with the single-phase XRD pattern, this observation supports incorporation of the five cations into a common rock-salt solid-solution lattice.

Collectively, these results establish a compositionally controlled comparative model system in which MO and HEO have the same nominal cation composition but distinct phase constitutions and elemental distributions. This contrast provides the structural basis for examining how phase separation versus integration into a common multication lattice influences subsequent aqueous corrosion behavior.

Just Accepted

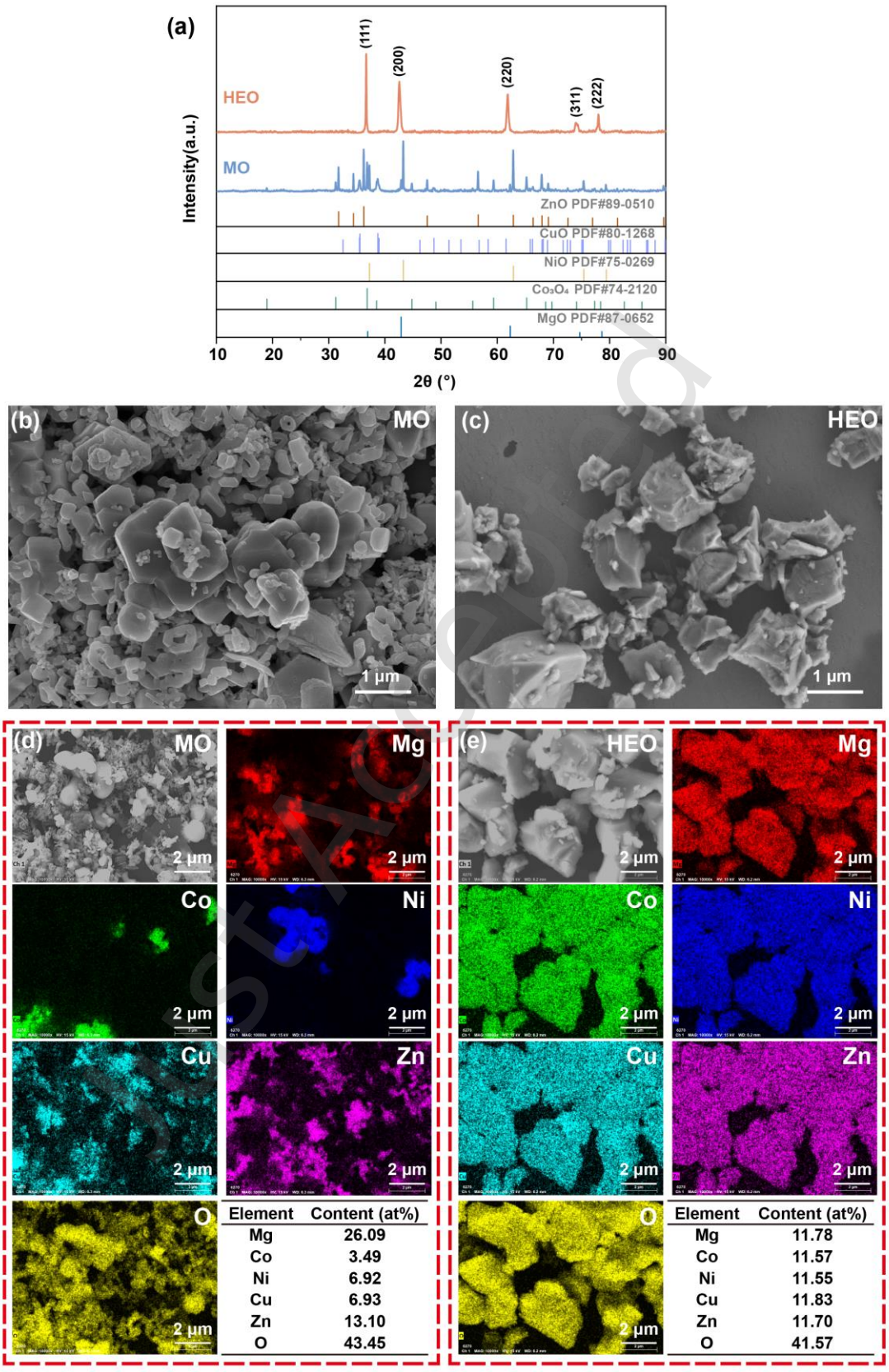


Fig. 3 Initial phase constitution and microstructural characteristics of MO and HEO powders: (a) XRD patterns; (b, c) SEM images of MO and HEO, respectively; and (d, e) EDS elemental maps of MO and HEO showing the distributions of Mg, Co, Ni, Cu, Zn and O. The accompanying tables list the

corresponding element contents.

3.2. Macroscopic corrosion behavior under different hydrochloric acid concentrations

Figure 4 summarizes the macroscopic corrosion responses of MO and HEO after immersion in 1 and 6 M HCl for 12 h. As shown in Fig. 4a-f, the initial MO and HEO powders exhibited distinctly different appearances. After immersion, the recovered powders showed visible changes, with MO becoming more uniform in color while HEO retained a comparatively homogeneous dark appearance. These observations indicate distinct macroscopic responses of MO and HEO to acid exposure.

The corresponding mass-loss results (Fig. 4g) reveal a pronounced concentration-dependent crossover in the relative corrosion behavior of MO and HEO. In 1 M HCl, both materials degraded substantially, but HEO showed lower net mass loss than MO. When the HCl concentration was increased to 6 M, the net mass loss of MO increased only slightly to 64.01 ± 9.19%, whereas that of HEO increased sharply to 85.58 ± 11.22%, exceeding that of MO. Thus, HEO exhibited lower net mass loss than MO in 1 M HCl, but a substantially higher value in 6 M HCl. This crossover indicates that forming a single-phase high-entropy solid solution does not necessarily reduce net mass loss and that its corrosion response depends strongly on acid concentration. To characterize the bulk solution acidity associated with these contrasting corrosion responses, Fig. 4h compares the pH values before and after immersion. Both the MO and HEO solutions remained strongly acidic after 12 h in 1 and 6 M HCl.

The initial particle characteristics of MO and HEO may also contribute to the measured gravimetric response. SEM-based analysis showed that HEO possessed a larger apparent particle size than MO (Fig. S1), with average particle sizes of 0.74 and 0.27 μm, respectively. The BET specific surface areas

Just Accepted

of the initial MO and HEO powders were 6.620 and 1.260 m^2/g, respectively. Larger particles would be expected to reduce apparent HEO degradation under powder-immersion conditions by lowering the specific surface area exposed to the acid. Such a size effect is also consistent with the gravimetric differences among the individual-oxide references (Fig. S3), which may partly reflect variations in their initial particle morphology and size (Fig. S2). However, particle size alone cannot account for the concentration-dependent crossover, because HEO exhibited substantially greater net mass loss than MO in 6 M HCl despite its larger particle size. Particle size may therefore contribute to the mass-loss differences, but it is insufficient on its own to explain the crossover. Its origin is further examined through element-specific dissolution (Section 3.3) and post-corrosion phase evolution (Section 3.4). It should also be noted that the measured net mass loss represents a net change in the recovered solid mass rather than the amount of material dissolved directly. Oxide dissolution, retention or precipitation of corrosion-derived solids, and powder recovery during post-immersion processing can influence the recovered solid mass.

Just Accepted

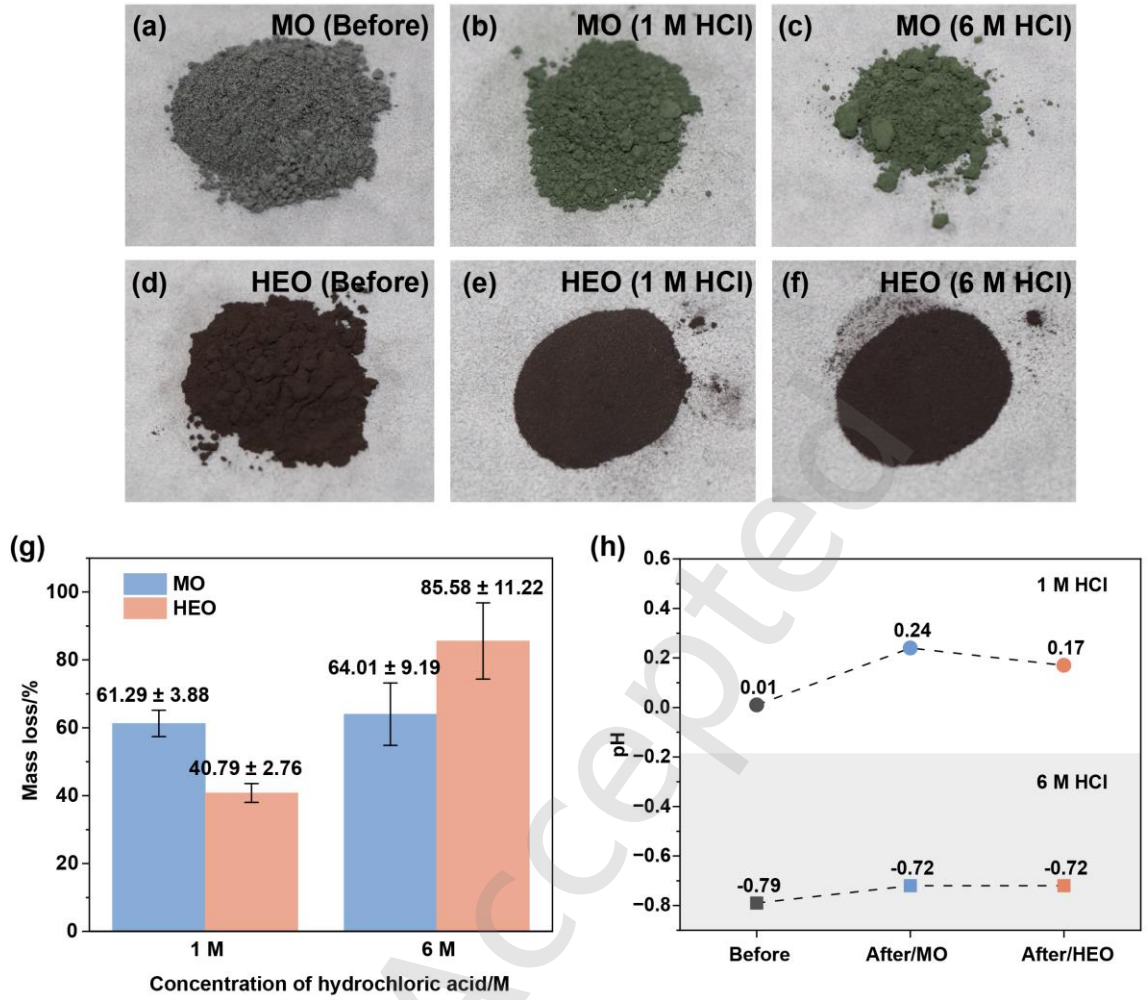


Fig. 4 Macroscopic appearance and corrosion response of MO and HEO before and after immersion in 1 M and 6 M HCl: (a, d) initial MO and HEO powders; (b, c) recovered MO powders after immersion in 1 and 6 M HCl; (e, f) recovered HEO powders after immersion in 1 and 6 M HCl; (g) net mass loss after 12 h; (h) solution pH before and after corrosion. The mass-loss values are presented as the mean ± standard deviation from three independent experiments.

3.3. Phase-dependent elemental dissolution

Element-specific dissolution was quantified using the element dissolved fraction (K_i), defined as

$$K_i = \frac{n_{i,dissolved}}{n_{i,initial}} \quad (1)$$

where $n_{i,dissolved}$ is the amount of element i detected in the corrosion solution after immersion, calculated from its ICP-OES concentration and the solution volume, and $n_{i,initial}$ is its initial amount in the tested powder. Thus, K_i provides a common basis for comparing the extent of elemental dissolution among

Just Accepted

the individual-oxide references, MO, and HEO (Fig. 5a). The corresponding elemental concentrations determined by ICP-OES are summarized in Table 1. Thus, K_i represents the net fraction of element *i* remaining dissolved in the corrosion solution at the end of immersion.

The individual-oxide references exhibited strongly differentiated dissolution responses under the present immersion conditions (Fig. 5a). MgO, CuO, and ZnO were extensively dissolved, whereas NiO and Co_3O_4 showed only limited dissolution. This first-order separation persisted at both acid concentrations. The contrast became particularly pronounced in 6 M HCl, where MgO, CuO, and ZnO approached complete dissolution but the K_i of NiO and Co_3O_4 remained below 0.01. These measurements serve a dual purpose in the present analysis. First, they provide a constituent-level reference for distinguishing the more extensively dissolved oxides from the relatively persistent ones under the same immersion conditions. Second, they allow us to test whether MO, in which the same oxides coexist as separate phases, retains the constituent-specific dissolution tendencies of the individual oxides, and whether incorporation of the same cations into the single-phase HEO lattice alters these tendencies. Because the individual oxide powders differed in their initial particle morphology and size (Fig. S2), the absolute values should be regarded as as-tested dissolution responses rather than an intrinsic ranking of oxide dissolution susceptibility. Nevertheless, the first-order separation between the extensively dissolved and the relatively persistent oxides is large enough to be used as a relative reference in the subsequent comparison.

MO exhibited pronounced constituent-specific dissolution under both acid concentrations. In 1 M HCl, the K_i followed the order Co < Ni << Mg < Zn < Cu, with Cu, Zn, and Mg being substantially more extensively dissolved than Ni and particularly Co. Increasing the HCl concentration to 6 M did

Just Accepted

not substantially alter this first-order separation, although the K_i of Ni increased. MO therefore retained the broad separation observed for the individual-oxide references, with substantially greater dissolution of Mg, Zn, and Cu than of Ni and Co. This correspondence suggests that MO retains the broad constituent-specific tendencies observed in the individual-oxide tests.

In contrast, incorporation of the same five cations into the single-phase HEO substantially narrowed the range of K_i (Fig. 5a). In 1 M HCl, this convergence of K_i resulted from decreases in the K_i of Mg, Cu, and Zn and increases in those of Ni and Co relative to MO. This reduced elemental dissolution selectivity coincided with the lower net mass loss of HEO relative to MO in 1 M HCl (Fig. 4g).

In 6 M HCl, HEO again exhibited substantially smaller differences in K_i, but the coupled multielement dissolution occurred at a markedly higher dissolution level. Relative to MO, the most pronounced changes were the increases in Ni and Co dissolution, whereas the changes in Mg, Cu, and Zn were comparatively smaller. To visualize these changes directly, the difference in mean K_i between HEO and MO was calculated as

$$\Delta K_i = K_i^{HEO} - K_i^{MO} \quad (2)$$

where positive and negative ΔK_i values indicate higher and lower K_i in HEO relative to MO, respectively (Fig. 5b). The ΔK_i values therefore show that the reduced elemental dissolution selectivity in HEO arises from opposite changes in the dissolution of different constituents. In 6 M HCl, this reduced elemental dissolution selectivity coincided with substantially greater, rather than lower, net mass loss of HEO (Fig. 4g).

Taken together, and consistent with their dual role defined above, the individual-oxide references and MO exhibit a similar first-order separation between the extensively dissolved Mg-, Zn-, and Cu-

Just Accepted

containing constituents and the relatively persistent Ni- and Co-containing constituents. Structural integration of the same cations into the common rock-salt phase substantially reduces these differences in elemental dissolved fractions. Importantly, the level toward which the K_i converge depends strongly on acid concentration: convergence occurs at comparatively low K_i in 1 M HCl but at substantially higher K_i in 6 M HCl. Reduced elemental dissolution selectivity can therefore be associated with either lower or higher overall net mass loss, depending on environmental aggressiveness.

Table 1 Dissolved elemental concentrations determined by ICP-OES after immersion of MO and HEO in 1 and 6 M HCl for 12 h.

Sample	Condition	Elemental concentrations (mM)				
		Mg	Co	Ni	Cu	Zn
MO	1 M HCl	74.03	0.18	1.71	90.11	75.59
HEO	1 M HCl	32.35	37.86	33.97	30.67	34.27
MO	6 M HCl	71.59	0.38	13.91	88.91	75.50
HEO	6 M HCl	62.71	78.48	69.69	71.43	66.17

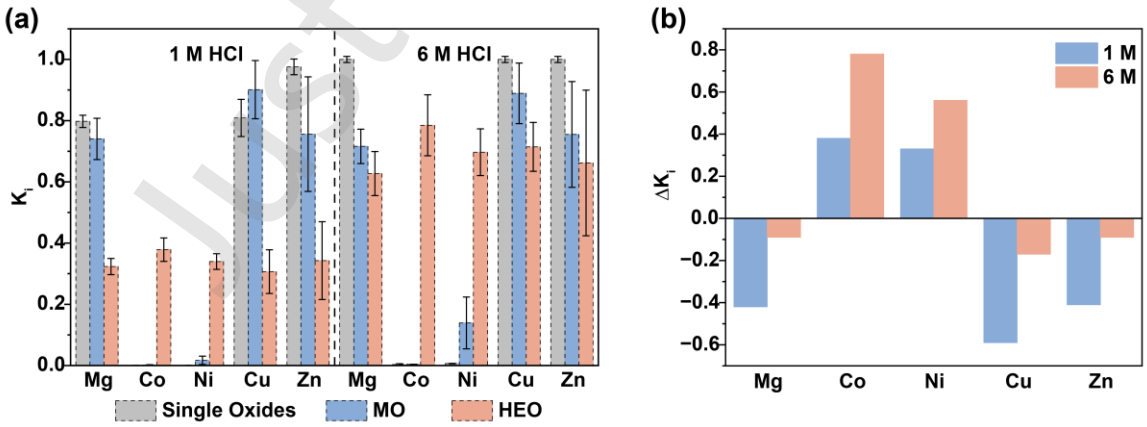


Fig. 5 Element-specific dissolution characteristics of the individual-oxide references, MO, and HEO after immersion in 1 and 6 M HCl for 12 h: (a) element dissolved fractions (K_i) of Mg, Co, Ni, Cu, and Zn, expressed as the mean ± standard deviation of three independent experiments; and (b) difference in mean elemental dissolved fractions between HEO and MO (ΔK_i).

3.4. Phase evolution after acid corrosion

Just Accepted

Figure 6 presents the XRD patterns of MO and HEO before and after corrosion in HCl solutions, revealing distinctly different phase evolution of the residual solids. For MO (Fig. 6a), the pristine sample exhibits diffraction peaks corresponding to the individual oxide phases, including MgO, Co_3O_4, NiO, CuO, and ZnO. After corrosion, the diffraction peaks of MgO, CuO, and ZnO disappear or are significantly weakened, whereas the reflections of NiO and Co_3O_4 remain detectable. This phase evolution is consistent with the ICP-OES results for the corrosion solution of MO, which show substantially greater K_i of Mg, Cu, and Zn than of Ni and Co (Fig. 5a). The preferential retention of NiO and Co_3O_4 therefore provides solid-state evidence consistent with the phase-dependent selective dissolution observed for MO.

In contrast, the diffraction patterns of the pristine and corroded HEO samples are dominated by reflections of the rock-salt (MgCoNiCuZn)O solid solution (Fig. 6b). After immersion in both 1 M and 6 M HCl, the characteristic diffraction peaks of the rock-salt phase remain visible, showing that the recovered HEO solids retain a detectable parent rock-salt phase. Importantly, persistence of the rock-salt diffraction pattern should not be interpreted as evidence of limited corrosion, particularly for HEO exposed to 6 M HCl, which exhibits substantial net mass loss. Rather, the XRD results indicate that the remaining solid retains the parent structure despite extensive material removal.

The HEO sample after corrosion in 1 M HCl shows weak additional diffraction features. Several of these reflections are consistent with a $Cu_2(OH)_3Cl$-type copper hydroxychloride phase, suggesting the presence of minor Cu/Cl-containing corrosion-derived species in the washed and dried residue (Fig. 6b). In contrast, no distinct secondary crystalline phase was resolved after exposure to 6 M HCl. However, the absence of detectable diffraction peaks does not exclude the presence of minor or poorly

Just Accepted

crystalline Cu/Cl-containing corrosion-derived species. The nature and spatial distribution of the corrosion-derived species are further examined by SEM/EDS in the following section.

Overall, MO and HEO exhibit distinctly different phase evolution after acid exposure. Selective removal of the more soluble oxide constituents in MO results in the relative retention of NiO and Co_3O_4, whereas the residual HEO retains the parent rock-salt structure despite substantial material loss. The additional weak reflections observed after exposure to 1 M HCl suggest the presence of minor secondary crystalline species in the washed and dried HEO residue. Together with the elemental dissolution results, these observations establish a clear association between phase constitution and the evolution of the residual crystalline phases during acid corrosion.

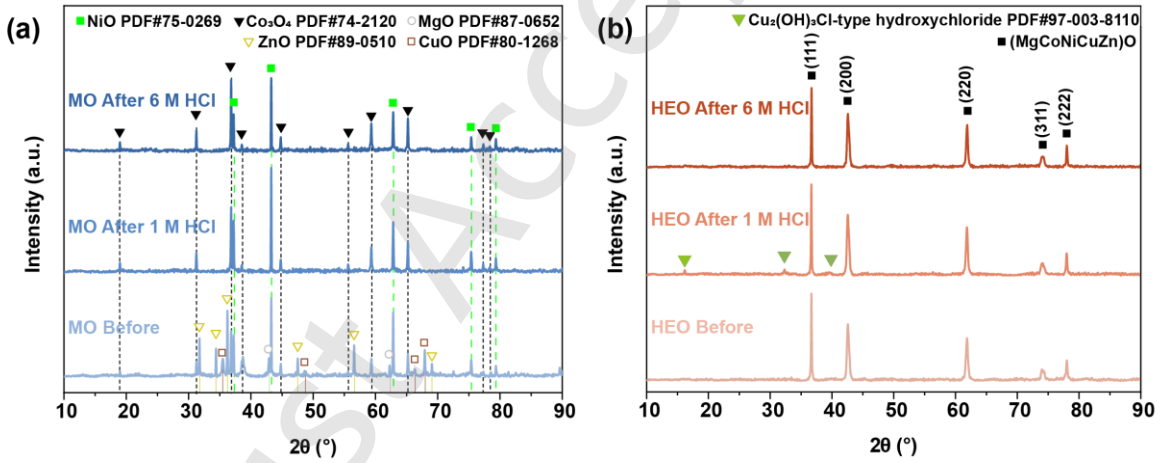


Fig. 6 XRD patterns showing the phase evolution of MO and HEO before and after immersion in 1 and 6 M HCl for 12 h: (a) MO and (b) HEO. In (b), inverted triangles mark the weak additional reflections observed in HEO after 1 M HCl exposure.

3.5. Post-corrosion morphology

Figure 7 shows the macroscopic appearance and interfacial stratification of MO and HEO after 12 h of immersion in 1 and 6 M HCl. As shown in Fig. 7a-d, MO produces relatively homogeneous colored solutions under both acid concentrations. HEO systems exhibit visible heterogeneity near the solid-liquid interface. Enlarged views of the HEO systems (Fig. 7e, f) further reveal clear macroscopic

Just Accepted

stratification under both 1 and 6 M HCl, with visually distinguishable residual oxide, inner and outer stratified regions, and the overlying corrosion solution. Although stratification is observed under both conditions, the color and spatial appearance of the stratified regions differ between 1 and 6 M HCl. Macroscopic observation alone cannot determine the chemical nature of these regions. The time-series photographs in Fig. S4 further show that the stratified appearance of the HEO systems becomes progressively more distinguishable during immersion, whereas no comparably pronounced stratification develops in MO.

SEM observations further reveal distinct post-corrosion morphologies of MO and HEO (Fig. 8). For MO, the residual particles remain morphologically heterogeneous under both conditions, with more evident surface roughening after exposure to 6 M HCl. HEO shows a clearer concentration-dependent change. After immersion in 1 M HCl, many particles retain relatively well-defined outlines with localized surface degradation. Exposure to 6 M HCl results in more widespread surface roughening and numerous fine particles attached to the larger residual particles. These morphological features are consistent with the contrasting residual-solid evolution indicated by the elemental dissolution and phase analyses above.

Their local elemental distributions provide further evidence of contrasting residual-solid evolution (Fig. 9). EDS mapping of representative MO regions after corrosion in both 1 and 6 M HCl reveals pronounced elemental heterogeneity, with the residual particles dominated by Ni and Co signals and only weak Mg, Cu, and Zn signals (Fig. 9a, b). The corresponding semi-quantitative EDS results further indicate relative enrichment of Ni and Co. This distribution is consistent with the low K_i of Ni and Co determined by ICP-OES (Fig. 5) and the persistence of NiO and Co_3O_4 reflections in the post-

Just Accepted

corrosion XRD patterns (Fig. 6a), collectively supporting the relative retention of Ni- and Co-rich oxide phases in the recovered MO solids.

In contrast, Mg, Co, Ni, Cu, and Zn remain detectable within the analyzed residual HEO particles after corrosion (Fig. 9c, d). After exposure to 1 M HCl, localized regions enriched in both Cu and Cl are observed, consistent with the Cu/Cl-containing corrosion-derived species indicated by the weak additional XRD reflections (Fig. 6b). Following exposure to 6 M HCl, localized Cl enrichment is also detected, primarily in association with some of the fine particles attached to the larger residual particles, whereas comparably pronounced Cu/Cl-rich regions are not observed.

Overall, MO and HEO exhibit distinct modes of residual-solid evolution after acid exposure. MO retains Ni- and Co-rich oxide phases after selectively removing more readily dissolved constituents. In contrast, the recovered HEO retains a multielement rock-salt phase accompanied by Cu/Cl-containing corrosion-derived species. These observations are consistent with the constituent-specific dissolution identified by ICP-OES and further highlight the distinct residual-solid evolution associated with the different phase constitutions of MO and HEO.

Just Accepted

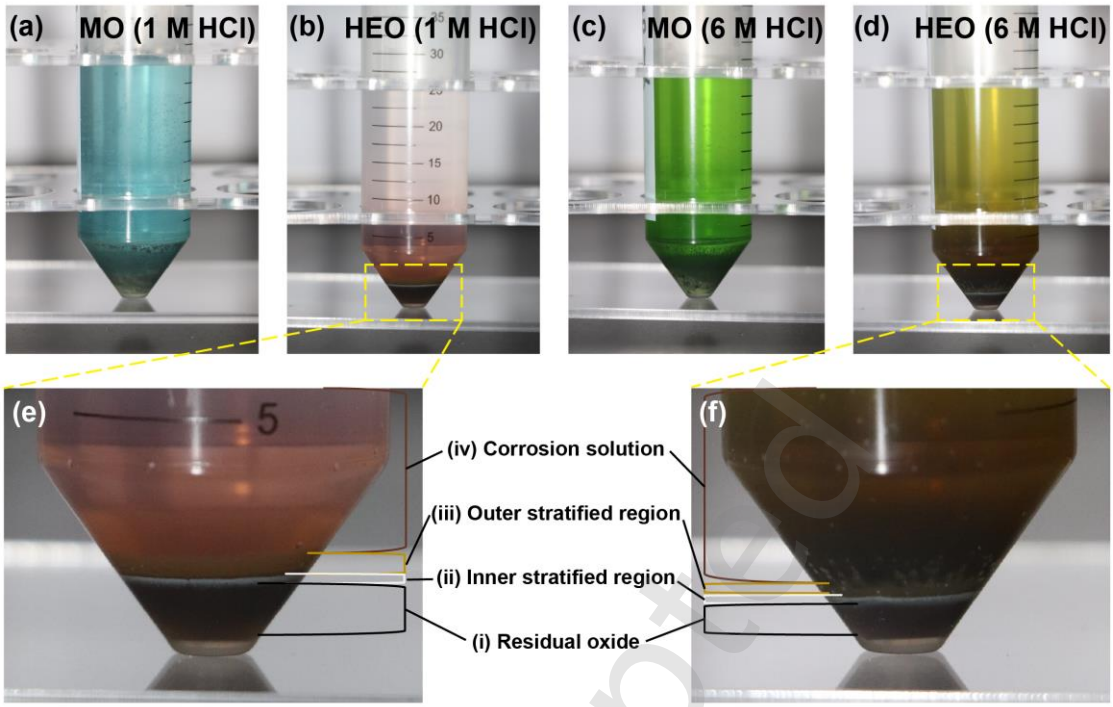


Fig. 7 Macroscopic appearance of MO and HEO after immersion in HCl for 12 h: (a) MO in 1 M HCl; (b) HEO in 1 M HCl; (c) MO in 6 M HCl; (d) HEO in 6 M HCl; (e, f) enlarged views of the boxed regions in (b, d), respectively, highlighting macroscopic stratification near the HEO solid-liquid interfaces.

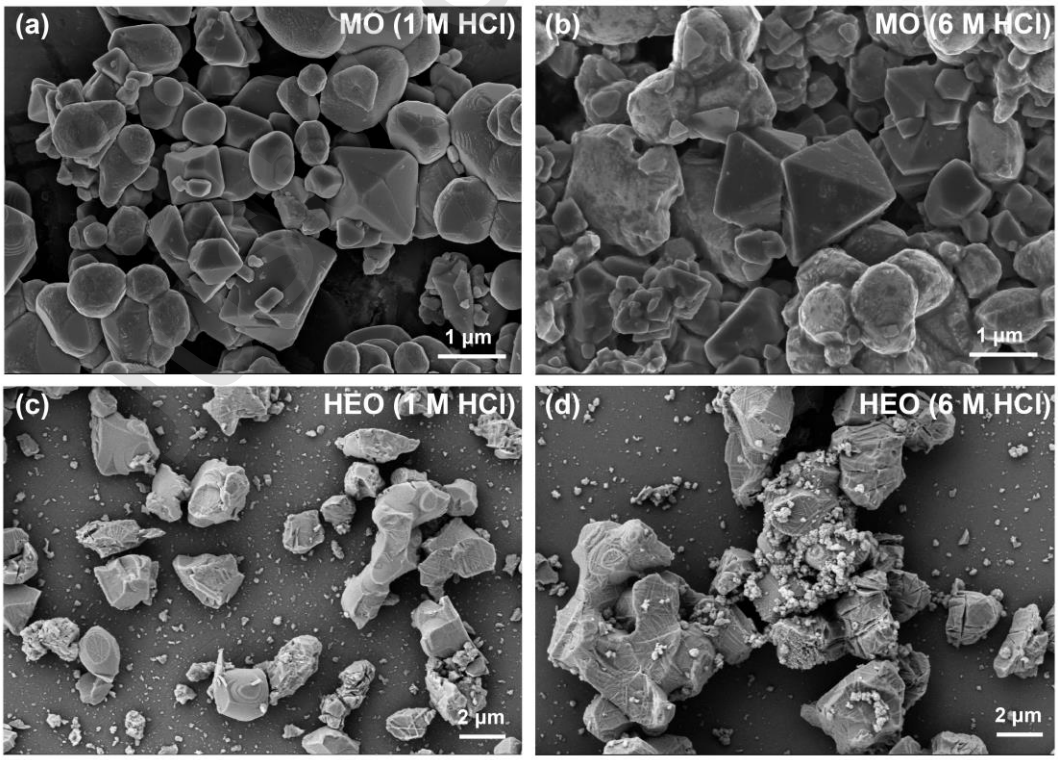


Fig. 8 SEM images of residual MO and HEO powders after immersion in HCl for 12 h: (a) MO in 1 M HCl; (b) MO in 6 M HCl; (c) HEO in 1 M HCl; and (d) HEO in 6 M HCl.

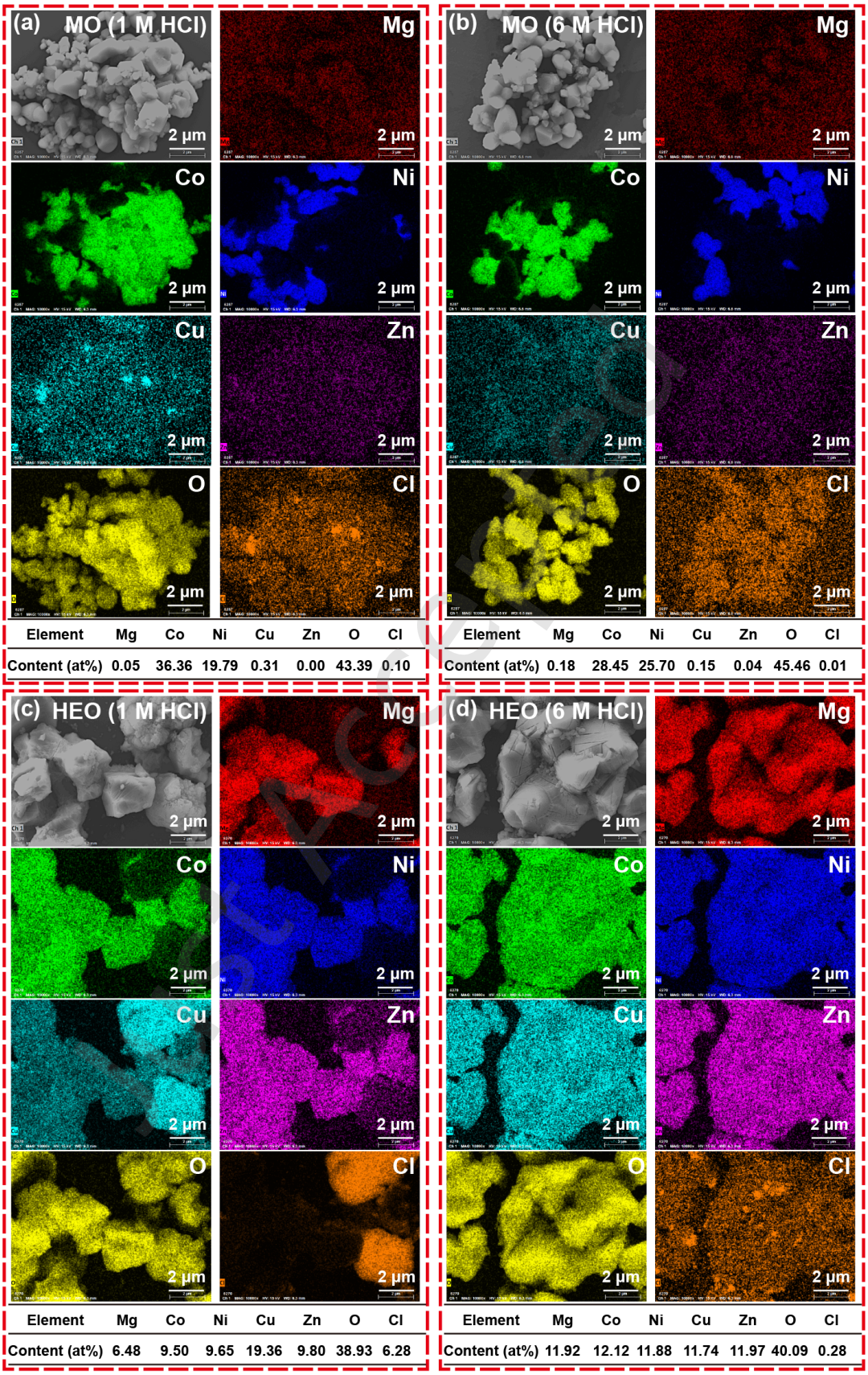


Fig. 9 EDS elemental maps of residual powders after immersion in HCl for 12 h: (a) MO in 1 M HCl; (b) MO in 6 M HCl; (c) HEO in 1 M HCl; and (d) HEO in 6 M HCl. The maps show the distributions

of Mg, Co, Ni, Cu, Zn, O and Cl. The accompanying tables list the corresponding element contents.

3.6. Corrosion mechanisms of MO and HEO

Building on the dissolution and residual-solid contrasts described above, the corrosion responses of MO and HEO can be explained by differences in cation accommodation and how their dissolution responses evolve with acid concentration (Fig. 10). In MO, the constituent oxides remain as independent phases, whereas in HEO the same five cations are incorporated into a common rock-salt solid-solution lattice [3,36]. This difference in phase constitution is associated with markedly different expressions of constituent-specific dissolution during acid exposure.

In MO, constituent-specific dissolution differences remain pronounced. Mg-, Zn-, and Cu-containing phases undergo substantially greater dissolution, whereas Ni- and Co-containing phases are preferentially retained. ICP-OES, XRD, and EDS analyses consistently support this interpretation. ICP-OES reveals substantially lower K_i of Ni and Co than of Mg, Cu, and Zn (Fig. 5), while post-corrosion XRD and EDS show the persistence of NiO- and Co_3O_4-rich residual phases (Figs. 6 and 9). The individual-oxide references show the same first-order separation between the more extensively dissolved Mg-, Zn-, and Cu-containing constituents and the more persistent Ni- and Co-containing constituents under the present immersion conditions, as established in Section 3.3. Corrosion of MO can therefore be described as a phase-dependent selective dissolution pathway in which constituent-specific dissolution responses remain largely independently expressed because the oxide components persist as separate phases.

HEO exhibits a distinctly different dissolution response. Incorporation of Mg, Co, Ni, Cu, and Zn into the common rock-salt phase is associated with a substantial narrowing of the differences among

Just Accepted

their K_i relative to MO. In 1 M HCl, relative to MO, the K_i of Mg, Cu, and Zn decrease, whereas those of Ni and Co increase, causing the five elements to converge toward a comparatively low dissolution level. In 6 M HCl, the differences among K_i remain small. Still, this narrowing occurs at a substantially higher dissolution level, with particularly pronounced increases in Ni and Co dissolution relative to MO (Fig. 5). Thus, structural integration into the common rock-salt phase is associated with less selective multielement dissolution, consistent with a coupled dissolution response. The overall extent of dissolution remains strongly dependent on acid concentration. First-principles calculations for the same entropy-stabilized oxide have shown that cation-vacancy formation energies depend strongly on local compositional and structural environments [37], providing independent evidence that cation stability within the shared lattice cannot be inferred simply from the corresponding binary oxides.

The residual-solid analyses support this interpretation. Unlike MO, no independent NiO or Co_3O_4 residual phases were detected by XRD in HEO after corrosion. Instead, a detectable parent rock-salt phase remains in the recovered HEO solids after exposure to both acid concentrations (Fig. 6). At the same time, EDS shows that Mg, Co, Ni, Cu, and Zn remain detectable within the analyzed residual particles (Fig. 9). The remaining crystalline solid retains the parent structural framework after substantial material removal. HEO also exhibits interfacial stratification (Fig. 7), while the XRD and EDS results indicate the presence of Cu/Cl-containing corrosion-derived species in the recovered solids. These features are more evident after exposure to 1 M HCl. Retention of corrosion-derived species may contribute to the lower net mass loss of HEO under this condition, although the magnitude of this contribution has not been quantified.

The concentration-dependent coupled multielement dissolution provides a basis for understanding

Just Accepted

the crossover in the macroscopic corrosion response. In 1 M HCl, the comparatively low dissolution level toward which the constituent responses converge coincides with lower net mass loss of HEO than that of MO. The larger initial particle size of HEO may also contribute to its lower net mass loss in 1 M HCl, and its contribution cannot be separated from that of phase constitution in the present comparison. In 6 M HCl, however, convergence occurs at substantially higher K_i, particularly because Ni and Co, which remain relatively persistent as independent oxides in MO, dissolve substantially more extensively once incorporated into the HEO lattice. This change coincides with the reversal in the relative net mass loss of HEO and MO, with HEO exhibiting substantially greater net mass loss than MO. The present results therefore distinguish elemental dissolution selectivity from overall corrosion resistance. Reducing differences among constituent dissolution responses does not necessarily reduce material degradation.

Overall, the corrosion behavior of MO and HEO follows two distinct, phase-dependent pathways. In phase-separated MO, constituent-specific dissolution differences remain pronounced, resulting in preferential removal of Mg-, Zn-, and Cu-containing phases and retention of Ni- and Co-rich residual phases. In single-phase HEO, although incorporation of the same cations into a common rock-salt lattice is associated with a narrower distribution of K_i, the level toward which these responses converge depends strongly on acid concentration. Collectively, for the two model materials compared here, phase constitution influences how constituent-specific dissolution responses are expressed, whereas acid concentration strongly influences the overall extent of dissolution and net mass loss.

Just Accepted

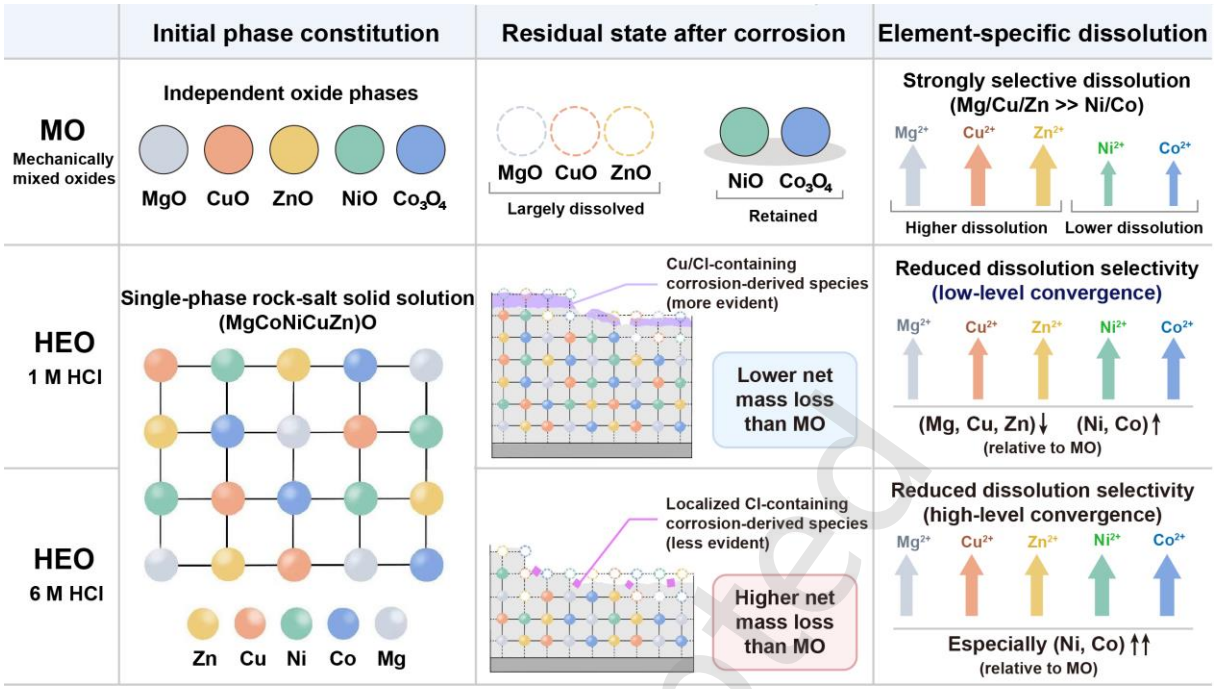


Fig. 10 Schematic illustration of the corrosion pathways of MO and HEO in HCl, highlighting selective dissolution in MO, concentration-dependent dissolution convergence in HEO, and the resulting differences in residual-solid evolution and net mass loss.

3.7. Implications of the core effects of high-entropy materials for corrosion-resistant ceramic design

The present comparison provides a basis for re-examining the relevance of the four core effects to aqueous corrosion. The four core effects were originally developed primarily to rationalize phase stability, diffusion, and mechanical behavior, particularly at elevated temperatures [11]. Their relevance to ambient aqueous corrosion is therefore less direct. Acid corrosion of oxides is governed primarily by interfacial processes, including proton adsorption, disruption of M-O coordination, cation detachment, and the evolution of corrosion-derived species [38,39]. Accordingly, the four core effects should not be treated as independent mechanisms that inherently improve corrosion resistance, but rather as structural and chemical factors that may modify different stages of the corrosion pathway.

As shown in Section 3.6, MO and HEO differ fundamentally in whether the constituent oxides retain

Just Accepted

independent phase identities or share a common rock-salt lattice. For HEO, the most direct implication of high-entropy effect or configurational-entropy stabilization is precisely the formation of such a multicomponent single-phase structure [3]. This common-lattice architecture provides a structural basis for the substantially reduced elemental dissolution selectivity observed in HEO. Thus, high-entropy effect or configurational-entropy stabilization is most relevant to the present study through the formation of a single-phase structure, although its corrosion consequences still depend on solution aggressiveness.

If operative, the sluggish-diffusion effect could limit near-surface elemental migration within the shared lattice and thus influence the evolution of compositional gradients and interfacial products [11,40]. However, the present dissolution data provide no direct evidence for such a contribution, and sluggish diffusion is therefore not invoked to explain the reduced elemental dissolution selectivity of HEO.

Severe lattice distortion provides another possible connection between high-entropy structure and interfacial reactivity. High-entropy oxides contain heterogeneous local coordination, strain, and defect environments [37,41], and local strain can substantially modify vacancy-formation energetics [37]. Because oxide dissolution is also sensitive to surface coordination and proton-assisted disruption of M–O bonds [42], different local configurations may exhibit different susceptibilities to acid attack. The resulting corrosion consequence is not necessarily beneficial: favorable or unfavorable effects depend on the specific local atomic configuration and solution chemistry.

The cocktail effect describes emergent and non-additive properties arising from interactions among multiple constituent elements and their structural and chemical environments [10,11]. The crossover

Just Accepted

between MO and HEO shows that formation of a common lattice does not simply average or improve the corrosion resistance of the constituent oxides. A similar departure from simple compositional averaging has been reported in CMAS corrosion of high-entropy rare-earth phosphates, where the response remained sensitive to constituent-specific chemical factors [29]. Together with the present results, this indicates that multicomponent coupling modifies the expression of constituent-specific chemical tendencies within a shared structural environment. On this basis, the present results and related observations in other high-entropy oxide systems suggest that the corrosion consequence of the cocktail effect depends on composition-specific interactions and environmental conditions rather than on configurational entropy alone, and therefore need not be universally beneficial.

This interpretation suggests that the composition of corrosion-resistant HECs could be deliberately tuned to promote preferential reactions of selected constituents with the service environment. Such reactions could potentially generate stable, adherent, transport-limiting surface products while preserving the structural integrity of the underlying multicomponent lattice. This idea parallels the formation of protective Cr_2O_3 scales during alloy oxidation [43] and the role of corrosion-resistant alloying elements in stabilizing passive films in aqueous environments [44]. However, this is a design hypothesis rather than a demonstrated mechanism. The Cu/Cl-containing species observed here suggest that compositional design may influence near-surface reaction chemistry, although their protective function has yet to be established.

Accordingly, assessing the corrosion resistance of HECs requires considering three coupled factors: the intrinsic stability of each constituent in the target medium, changes in dissolution behavior after incorporating the constituents into a common lattice, and the aggressiveness of the service environment.

Just Accepted

Composition and phase-constitution design should thus aim at minimizing material loss under a defined service environment, and whether high-entropy solid-solution formation improves corrosion resistance must be evaluated case by case. High-entropy engineering therefore provides a strategy for tailoring elemental dissolution behavior and corrosion pathways to specific service environments.

4 Conclusion

By comparing an entropy-stabilized rock-salt (MgCoNiCuZn)O (HEO) high-entropy oxide with a mechanically mixed oxide (MO) of identical nominal cation composition, this study shows that high-entropy solid-solution formation modifies corrosion pathways during immersion in 1 and 6 M HCl, with the resulting corrosion response strongly dependent on acid concentration. In MO, the independent oxide phases dissolve selectively, with Mg-, Zn-, and Cu-containing phases removed preferentially and Ni- and Co-containing phases retained. In HEO, the same cations share a rock-salt lattice and exhibit coupled multielement dissolution, with the dissolution level of this coupling increasing markedly with acid concentration. This concentration dependence produces a crossover, with HEO losing less mass than MO in 1 M HCl but more in 6 M HCl. These findings indicate that reduced elemental dissolution selectivity does not necessarily mean improved corrosion resistance, and that the corrosion performance of high-entropy ceramics is governed by the interplay among phase constitution, constituent chemistry, and environmental aggressiveness. Further studies are needed to determine whether the Cu/Cl-containing, corrosion-derived species observed here can be deliberately engineered into protective surface products, and to extend this phase-constitution-resolved comparison to other high-entropy oxide systems and service environments.

Just Accepted

Acknowledgements

The present work was financially supported by the National Natural Science Foundation of China (No. 52371023, 52332003, 52032001).

Author contributions

Ying Zhao: Writing-original draft, Investigation, Data curation, Formal analysis. **Ji-Xuan Liu:** Writing-review & editing, Supervision, Methodology, Funding acquisition. **Guo-Jun Zhang:** Writing-review & editing, Conceptualization, Supervision, Funding acquisition.

Availability of data and materials

The data that support the findings of this study are available from the corresponding author upon reasonable request.

Competing interests

The authors have no competing interests to declare that are relevant to the content of this article. The authors Ji-Xuan Liu and Guo-Jun Zhang are the Editorial Committee members of this journal.

Just Accepted

References

[1] Yeh JW, Chen SK, Lin SJ, *et al.* Nanostructured High-Entropy Alloys with Multiple Principal Elements: Novel Alloy Design Concepts and Outcomes. *Adv Eng Mater* 2004, **6**: 299–303.
[2] Cantor B, Chang ITH, Knight P, *et al.* Microstructural development in equiatomic multicomponent alloys. *Mater Sci Eng A* 2004, **375–377**: 213–218.
[3] Rost CM, Sachet E, Borman T, *et al.* Entropy-stabilized oxides. *Nat Commun* 2015, **6**: 8485.
[4] Sarker P, Harrington T, Toher C, *et al.* High-entropy high-hardness metal carbides discovered by entropy descriptors. *Nat Commun* 2018, **9**: 4980.
[5] Jin T, Sang X, Unocic RR, *et al.* Mechanochemical-assisted synthesis of high-entropy metal

nitride via a soft urea strategy. *Adv Mater* 2018, **30**: 1707512.
[6] Gild J, Zhang Y, Harrington T, *et al.* High-Entropy Metal Diborides: A New Class of High-Entropy Materials and a New Type of Ultrahigh Temperature Ceramics. *Sci Rep* 2016, **6**: 37946.
[7] Gild J, Braun J, Kaufmann K, *et al.* A high-entropy silicide: $(Mo_{0.2}Nb_{0.2}Ta_{0.2}Ti_{0.2}W_{0.2})Si_2$. *J Materiomics* 2019, **5**: 337–343.
[8] Qin Y, Liu JX, Li F, *et al.* A high entropy silicide by reactive spark plasma sintering. *J Adv Ceram* 2019, **8**: 148–152.
[9] Oses C, Toher C, Curtarolo S. High-entropy ceramics. *Nat Rev Mater* 2020, **5**: 295–309.
[10] George EP, Raabe D, Ritchie RO. High-entropy alloys. *Nat Rev Mater* 2019, **4**: 515–534.
[11] Miracle DB, Senkov ON. A critical review of high entropy alloys and related concepts. *Acta Mater* 2017, **122**: 448–511.
[12] Hsu WL, Tsai CW, Yeh AC, *et al.* Clarifying the four core effects of high-entropy materials. *Nat Rev Chem* 2024, **8**: 471–485.
[13] Shi Y, Yang B, Liaw P. Corrosion-resistant high-entropy alloys: A review. *Metals* 2017, **7**: 43.
[14] Qiu Y, Thomas S, Gibson MA, *et al.* Corrosion of high entropy alloys. *npj Mater Degrad* 2017, **1**: 15.
[15] Tang Z, Huang L, He W, *et al.* Alloying and Processing Effects on the Aqueous Corrosion Behavior of High-Entropy Alloys. *Entropy* 2014, **16**: 895–911.
[16] Wang Z, Liu ZX, Jin J, *et al.* Selective corrosion mechanism of CoCrFeMoNi high-entropy alloy in the transpassive region based on the passive film characterization by ToF-SIMS. *Corros Sci* 2023, **218**: 111206.
[17] Hou Y, Gharbi O, Xie C, *et al.* Tracking element-specific dissolution during pitting corrosion: an operando ICP-AES–electrochemical study of the CoCrFeMnNi Cantor alloy. *npj Mater Degrad* 2026, **10**: 33.
[18] Hu Q, Ye CP, Zhang SC, *et al.* Mo content-depended competition between Cr_2O_3 enrichment and selective dissolution of CoCrFeNiMox high entropy alloys. *npj Mater Degrad* 2022, **6**: 97.
[19] Yang J, Zeng Y, Zhu M, *et al.* Study on effect of chloride and temperature on corrosion behavior of CoCrFeMnNi high entropy alloy. *Int J Electrochem Sci* 2023, **18**: 100132.
[20] Ye B, Wen T, Liu D, *et al.* Oxidation behavior of $(Hf_{0.2}Zr_{0.2}Ta_{0.2}Nb_{0.2}Ti_{0.2})C$ high-entropy ceramics at 1073-1473 K in air. *Corros Sci* 2019, **153**: 327–332.
[21] Backman L, Gild J, Luo J, *et al.* Part I: Theoretical predictions of preferential oxidation in refractory high entropy materials. *Acta Mater* 2020, **197**: 20–27.
[22] Yan ZH, Liu JX, Peng P, et al. Oxidation resistance of equimolar multicomponent transition metal carbide solid solution. Adv Ceram 2024, **45**: 541–557.
[23] Cai F, Ni D, Bao W, *et al.* Ablation behavior and mechanisms of $Cf/(Ti_{0.2}Zr_{0.2}Hf_{0.2}Nb_{0.2}Ta_{0.2})C$–SiC high-entropy ceramic matrix composites. *Compos B Eng* 2022, **243**: 110177.
[24] Cao Y, Liu JX, Cheng W, *et al.* Oxidation of multi-principal component diborides at 2300 ℃ under ultrafast heating. *J Adv Ceram* 2026, 15: 9221361.
[25] Xu L, Gao H, He X, *et al.* Understanding the CMAS corrosion behavior of high-entropy $(La_{0.2}Sm_{0.2}Er_{0.2}Y_{0.2}Yb_{0.2})_2Ce_2O_7$. *J Am Ceram Soc* 2025, **108**: e20355.
[26] Zhou X, Liu JX, Tu TZ, *et al.* CMAS corrosion behavior of a high-entropy rare-earth aluminate ceramic prepared by atmospheric plasma spraying. *J Eur Ceram Soc* 2026, **46**: 118332.

Just Accepted

[27] Tu TZ, Liu JX, Zhou L, *et al.* Graceful behavior during CMAS corrosion of a high-entropy rare-earth zirconate for thermal barrier coating material. *J Eur Ceram Soc* 2022, **42**: 649–657.
[28] Fan W, Yang X, Li H, et al. Pressureless sintering of $(Y_{0.2}Gd_{0.2}Er_{0.2}Yb_{0.2}Lu_{0.2})_2Zr_2O_7$ high-entropy ceramic and its high temperature CMAS corrosion resistance. J Inorg Mater 2025, **40**: 159–167.
[29] Majee BP, Bryce K, Huang L, *et al.* A high-entropy rare-earth phosphate and its principle single component $REPO_4$ for environmental barrier coatings. *J Adv Ceram* 2025, **14**: 9221041.
[30] Fan Y, Bai Y, He X, *et al.* Revealing corrosion mechanisms and enabling predictive lifetime assessment of high-entropy rare-earth disilicates with superior CMAS corrosion resistance. *J Adv Ceram* 2026, **15**: 9221251.
[31] Wang Z, Sun L, Du T, *et al.* Insight into the synergistic effect of rare-earth elements on the CMAS corrosion behavior in $(RE_{1/4}Tm_{1/4}Yb_{1/4}Lu_{1/4})_2Si_2O_7$ (RE = Gd, Ho, and Sc) materials at 1300 °C. *J Adv Ceram* 2026, **15**: 9221330.
[32] Xue Y, Zhao X, An Y, *et al.* Corrosion behavior of high-entropy $(La_{0.2}Nd_{0.2}Sm_{0.2}Eu_{0.2}Gd_{0.2})Ce_2O_7$ in different aggressive molten salt. *Corros Sci* 2022, **204**: 110414.
[33] Fu S, Lin K, Gao Z, *et al.* Thermophysical properties and corrosion behavior against Na_2SO_4-V_2O_5 of cerate high-entropy ceramics. *J Eur Ceram Soc* 2026, **46**: 118314.
[34] Zhou L, Li F, Liu JX, *et al.* High-entropy A2B2O7-type oxide ceramics: A potential immobilising matrix for high-level radioactive waste. *J Hazard Mater* 2021, **415**: 125596.
[35] Brahlek M, Gazda M, Keppens V, *et al.* What is in a name: Defining "high entropy" oxides. *APL Mater* 2022, **10**: 110902.
[36] Almishal SSI, Sivak JT, Kotsonis GN, *et al.* Untangling individual cation roles in rock salt high-entropy oxides. *Acta Mater* 2024, **279**: 120289.
[37] Chae S, Williams L, Lee J, *et al.* Effects of local compositional and structural disorder on vacancy formation in entropy-stabilized oxides from first-principles. *npj Comput Mater* 2022, **8**: 95.
[38] Brown GE, Henrich VE, Casey WH, *et al.* Metal oxide surfaces and their interactions with aqueous solutions and microbial organisms. *Chem Rev* 1999, **99**: 77–174.
[39] Wang J. Thermodynamic equilibrium and kinetic fundamentals of oxide dissolution in aqueous solution. *J Mater Res* 2020, **35**: 898–921.
[40] Divinski SV, Pokoev AV, Esakkiraja N, *et al.* A mystery of "sluggish diffusion" in high-entropy alloys: The truth or a myth? *Diffus Found* 2018, **17**: 69–104.
[41] Kaufman J, Esfarjani K. Tunable lattice distortion in $MgCoNiCuZnO_5$ entropy-stabilized oxide. *J Mater Res* 2021, **36**: 1615–1623.
[42] Klyukin K, Rosso KM, Alexandrov V. Iron dissolution from goethite (α-FeOOH) surfaces in water by ab initio enhanced free-energy simulations. *J Phys Chem C* 2018, **122**: 16086–16091.
[43] Xie Y, Huang Y, Li Y, *et al.* A novel method to promote selective oxidation of Ni-Cr alloys: Surface spreading α-Al_2O_3 nanoparticles. *Corros Sci* 2021, **190**: 109717.
[44] Hashimoto K, Asami K, Kawashima A, *et al.* The role of corrosion-resistant alloying elements in passivity. *Corros Sci* 2007, **49**: 42–52.

Just Accepted